Topological Acoustic Delay Line

Zhiwang Zhang,[1] Ye Tian,[1] Ying Cheng,[1,*] Qi Wei,[1] Xiaojun Liu,[1,†] and Johan Christensen[2,‡]
[1]*Key Laboratory of Modern Acoustics, Department of Physics and Collaborative Innovation Center of Advanced Microstructures, Nanjing University, Nanjing 210093, China*
[2]*Universidad Carlos III de Madrid, ES-28916 Leganés, Madrid, Spain*

(Received 27 September 2017; revised manuscript received 5 February 2018; published 28 March 2018)

Topological protected wave engineering in artificially structured media is at the frontier of ongoing metamaterials research that is inspired by quantum mechanics. Acoustic analogues of electronic topological insulators have recently led to a wealth of new opportunities in manipulating sound propagation with strikingly unconventional acoustic edge modes immune to backscattering. Earlier fabrications of topological insulators are characterized by an unreconfigurable geometry and a very narrow frequency response, which severely hinders the exploration and design of useful devices. Here we establish topologically protected sound in reconfigurable phononic crystals that can be switched on and off simply by rotating its three-legged "atoms" without altering the lattice structure. In particular, we engineer robust phase delay defects that take advantage of the ultrabroadband reflection-free sound propagation. Such topological delay lines serve as a paradigm in compact acoustic devices, interconnects, and electroacoustic integrated circuits.

DOI: 10.1103/PhysRevApplied.9.034032

I. INTRODUCTION

The discoveries of the quantum Hall effect [1,2], the quantum spin Hall effect [3,4], and topological insulators (TIs) [5–7] have paved the way toward novel topological states in condensed matter physics and stimulated the search for analogous topological systems with classical waves such as light [8–22], sound [23–36], and mechanical waves [37–39]. Early pioneering approaches to construct acoustic topological states in 2D systems relied on enforced circulating fluid flow in the background [23–26,40] to mimic the quantum Hall effect, whereas Floquet topological insulators have been realized in preset coupled ring-resonator waveguides [27,28,35]. Phononic "graphene" with double Dirac cones [30,31,34,36] can map the quantum spin Hall effect, and C_{3v} phononic crystals composed of anisotropic rods constitute acoustic valley Hall topological insulators [32,41–50]. However, an even greater challenge is posed by the lack of tunability and adaptation to functional needs which is essential for real-world applications that yet is an unexplored territory for topological acoustics in artificially structured media. Structures permitting defect-immune broadband acoustic signal processing have the possibility to significantly push forward important applications.

The purpose of this work is to demonstrate reconfigurable acoustic topological edge states in a phononic crystal (PC) without utilizing external bias. In doing so, we mimic the quantum valley Hall effect that exploits valley states as opposed to spin states. In the field of electronics, the angular rotation of the electron wave function at the K or K' point of the band structure generates an intrinsic magnetic moment analogous to that produced by the electron spin [41,42,45]. Analogously, vortex chirality adds a new degree of freedom (d.o.f.) to manipulate sound as provided through the orbital angular momentum [34,39,49]. We demonstrate that the direction of sound propagation at the K or K' point [i.e., right- or left-hand circularly polarized (RCP and LCP)] plays the role of the pseudospin d.o.f. in a 2D acoustic system. Breaking of the appropriate point group and translational symmetries can provide a general approach to pseudomagnetic fields [33,51,52] for Dirac quasiparticles. However, in our setup where the C_3 symmetry is preserved while the mirror symmetry is broken, there are not any pseudomagnetic fields but rather a mass term. Breaking the mirror symmetry of the primitive cell is accomplished by simply rotating the "atoms"; see, also, Refs. [32,36]. This induces band inversion between different valley pseudospin d.o.f., which further leads to topological phase transitions [53,54]. Here, the orientation of the atoms is tunable allowing us to remotely reconfigure the edge states. Moreover, the scatterer's design is improved to boost the bandwidth of the topological band

*Corresponding author.
chengying@nju.edu.cn
†Corresponding author.
liuxiaojun@nju.edu.cn
‡Corresponding author.
johan.christensen@gmail.com

 © 2018 American Physical Society

gap. Finally, we experimentally realize topologically protected broadband delay lines based on engineered phase delay defects (PDDs) that constitute a platform for acoustic devices. The proposed approach provides diverse routes to construct acoustic valley pseudospin states, which have profound implications for the fascinating physics of acoustic TIs with versatile potential applications.

II. EXPERIMENTAL DETAILS

The three-legged rods of the PC are precision fabricated using epoxy resin via 3D printing. The fabricated PC sample consists of 400 rods embedded in an air matrix. The height of the rods, which are placed between two parallel plates of Plexiglass, is chosen to be 1.40 cm. In this scenario, the two-dimensional approximation is applicable since the planar waveguide supports the propagating mode uniformly along the rod axis for the wavelengths under consideration. The experiments are conducted by a loudspeaker (ENPILL PD-2121) with a gradual pipe to generate a point sound source. Cone-shaped sound-absorbing foam is mounted around the surrounding of the PC to minimize the boundary reflections by the open space. Local pressure fields are measured by inserting 1/4-inch condensed microphones (GRAS type 40PH) into the top plate at the designated positions. The outputs of the microphones are acquired by a digitizer (NI PXI-4498) and processed by LabVIEW software. A frequency scan is performed from 5 to 10.0 kHz with an increment of 0.01 kHz. Highly reliable readings of the pressure amplitude at each frequency are ensured by multiple measurements, from which we obtain the complex transmission and sound intensity by means of the transfer-matrix method.

III. RESULTS AND DISCUSSION

A. Acoustic valley pseudospin states and topological mode inversion

The presence of Dirac-like degenerate points is an important requirement for engineering a topological phase. The degeneracies at the high-symmetry points are preserved if the point group includes the C_{3v} symmetries [33]. This structure constitutes a well-established platform to support a single Dirac cone at the corners of the first Brillouin zone (BZ) (see Appendix A). Keeping the mirror symmetry of the primitive cell unchanged, the unperturbed (cylindrical) rods are simply replaced by perturbed rods made of epoxy resin with the rotation angle $\varphi = 0°$ and the lattice constant $a = 2.17$ cm. The shape of the rod is a three-legged atom of length $d = 0.85$ cm and width $h = 0.30$ cm as shown in Figs. 1(a) and 1(b). This crystalline structure is arranged by periodically repeating the primitive cell $\boldsymbol{C}$ containing one rod, and the unit vectors $\boldsymbol{a}_1$ and $\boldsymbol{a}_2$ defining the primitive cell. Because of the matched mirror symmetries between the lattice and triangular scatterers, the dispersion relation of such a hexagonal structure maintains

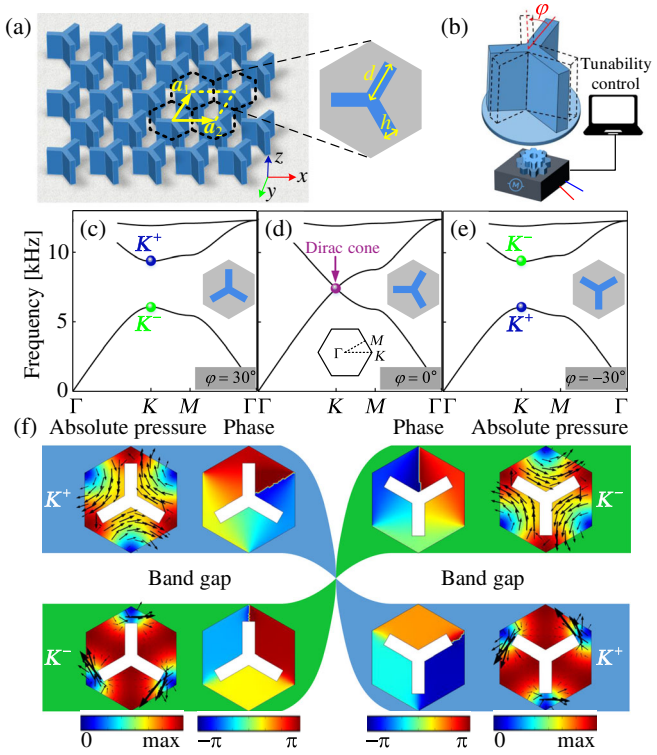

FIG. 1. Acoustic valley pseudospin states and topological mode inversion. (a) Schematics of the hexagonal lattice PC composed of perturbed TLRs embedded in an air matrix. (b) Symmetry breaking by rotating the rods attached to the computer-controlled electric motor. (c)–(e) Dispersion relations of the acoustic modes by reconfiguring the angle $\varphi = 30°$ (erected), $\varphi = 0°$ (degenerated), and $\varphi = -30°$ (upside down). The symbols K^+ and K^- denote the pseudospin states. (f) Topological mode inversion underlying the transition of pseudospin states. The rainbow color represents the amplitude of the absolute pressure and phase of the four pseudospin states. The arrows show the direction and amplitude of the intensity.

the Dirac cones at the corners of the first BZ at a finite frequency; see Fig. 1(d). We break the mirror symmetry of the primitive cell by simply rotating the three-legged rods (TLRs) [Fig. 1(b)] to obtain a controllable band gap separating different topological phases. To achieve structural tunability, computer-controlled motors are attached to the pedestals of the TLRs to provide the desired rotation. Two different symmetry-invariant geometries are created by breaking the mirror symmetry in two opposite ways: we build a unit cell composed of erected TLRs by rotating the rod to $\varphi = 30°$, and second, a unit cell composed of upside-down TLRs by rotating the rod to $\varphi = -30°$. In order to illustrate the mode-inversion process accompanied by a broken symmetry, we plot the dispersion relations as shown in Figs. 1(c)–1(e) (dispersion surfaces are plotted in Appendix A). Figures 1(c) and 1(e) display a pair of well-defined valleys at the corners of the first BZ, which are separated by an omnidirectional broad band gap spanning from 6073 to 9360 Hz. We demonstrate that the band gap is

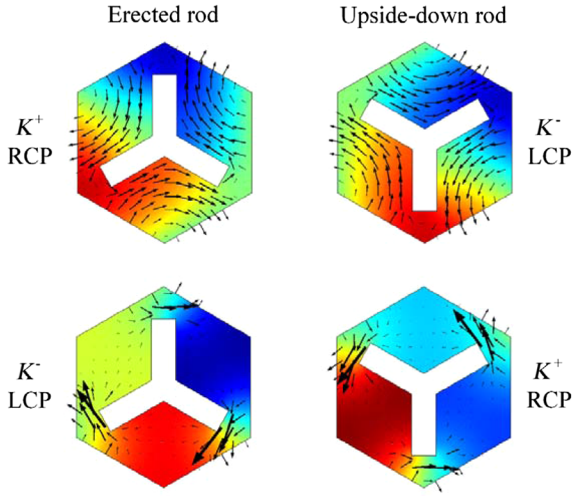

VIDEO 1. Dynamic views of the time-dependent spinning of intensity around the TLR with its respective RCP or LCP chirality. The rainbow color represents the amplitude of the total pressure of the four pseudospin states. The arrows show the direction and amplitude of the intensity.

drastically enlarged (see Appendix B). This band gap closes at $\varphi = 0°$ where the two modes become degenerate since the Γ-K symmetries of both crystal lattices and TLRs remain matched [Fig. 1(d)], implying that reopening of the band gap stems from breaking the C_{3v} symmetry. Rather than refabricating the PC to explore various topological states, we are able to fine-tune the topological transition when rotating the TLRs from $\varphi = -60°$ to $\varphi = 60°$ where a continuous gap closing and reopening process easily can be achieved (see Appendix C). In order to get an understanding of the physical picture behind the pseudospin states, we map the absolute pressure fields, intensity, and phase distributions of the states at the K point as shown in Fig. 1(f). These acoustic valley pseudospin states exhibit reversed chirality similar to electronic spin states. When the TLRs are erected in the hexagonal lattice, the acoustic vortex chirality is RCP (LCP) and labeled as $K^{+(-)}$ at the higher (lower) state as depicted in Fig. 1(f), left panel. When rotating the atoms to the upside-down configuration, the acoustic vortex chirality of the lower state changes to RCP (K^+) and the higher state changes to LCP (K^-) leading to an inverted band structure [Fig. 1(f), right panel]. The time-dependent spinning of intensity around the TLR with its respective RCP or LCP chirality is clearly visualized in Video 1. We emphasize that the pseudospin results from spectrally wide sound scattering in the PC containing broken mirror symmetry, which is much easier to design and reconfigure as opposed to fluid-circulator- or resonator-based schemes.

B. Broadband topological valley transport

We demonstrate that an interface between two acoustic TIs with different symmetry-broken geometries (erected and upside down) supports topologically protected edge states. We construct a phononic TI in a finite $20a \times 20a$ lattice as shown in Fig. 2(a). According to the band structure in Fig. 2(b), building a PC with either erected or upside-down TLRs prevents sound propagation as marked by the forbidden gray-shaded region that spans from 6100 to 9450 Hz. The topological edge states fall within the bulk band gap as indicated by the red solid line for positive interface and the blue dashed line for negative interface as seen in Fig. 2(b). The edge states originate from the change of the valley Chern index across the interface between topologically distinct regions. It has been shown that by means of an effective Hamiltonian [17,48,55,56], the nonvanishing valley Chern indices [56,57] $C^{(K,K')}$ can be determined by $2C^{(K,K')} = \pm 1 \times \mathrm{sgn}(\Delta_P)$. Here, Δ_P characterizes the geometrical perturbation, where its strength Δ_P depends on the rotation angle φ, and the sign of Δ_P depends on the orientation of the TLRs (see Appendix D). In the setup where the C_3 symmetry is preserved while the mirror symmetry is broken, there is not any gauge field but rather a mass term in the effective Hamiltonian [33], which can be also considered as the perturbation strength Δ_P. It can lead to helical edge states in the presence of domains walls where the mass (Δ_P) changes sign [32,50]. As a result, the interface with different signs of perturbation strength Δ_P will support the backscattering-immune transmission. For example, the negative interface shown in Fig. 2(b) has $\Delta_P < 0$ ($\Delta_P > 0$) in the erected (upside-down) region. Hence, there should be a backward-moving edge state at the K point due to $\Delta C^{(K)} = C^{(K)}_{\mathrm{upper}} - C^{(K)}_{\mathrm{lower}} = -1$, and a forward-moving edge state at the K' point due to $\Delta C^{(K')} = 1$. The simulated pressure fields at frequency $f = 7500$ Hz within the topological band gap are shown in Fig. 2(c) both for the topological edge states (structure I) and for bulk states (structure II). Here, sound waves are localized in the vicinity of the interface between the two TIs and decay exponentially away from it, proving that the bulk region is insulating due to the presence of band gaps therein. As shown in Fig. 2(d), we measure the transmission spectra for both structures under study. We observe a transmission enhancement of approximately 40 dB for the excitation of edge states (black line) as compared to the bulk states (red line), which unequivocally demonstrates that sound, when excited inside the band gap, does not evanescently tunnel through the bulk. Instead, sound waves couple to the edge mode and propagate unimpededly along the interface in the topological band gap. Note that a key feature of the topological edge states is the exponential decay of the field amplitude away from the interface. To experimentally confirm this feature, we further investigate the normalized pressure amplitude profile along a cutline in the middle of the crystal [red dashed line in Fig. 2(c)]. Figure 2(e) illustrates the measured profile of the edge state at frequency $f = 7500$ Hz, which agrees excellently with the simulation. The full width at half maximum (FWHM) of the envelope is $1.2a$, where a is the lattice

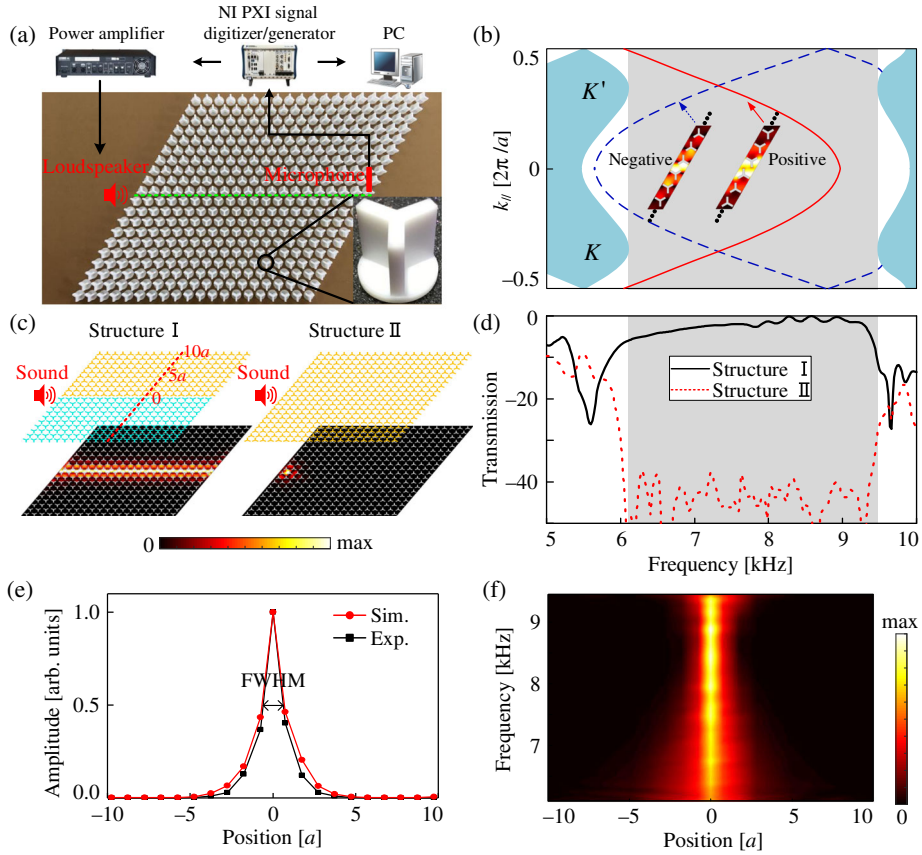

FIG. 2. Topologically protected edge waves localized at the interface within the PC created by different topological invariants. (a) Photograph of a fabricated PC sample (without the top cover). (b) Dispersion relation of the ribbon-shaped 2D PC with negative and positive interfaces comprising 20 cells on each side. Dark gray regions indicate the frequency range of the topological band gap. The solid red and dashed blue lines are for edge states with positive and negative interfaces. Inset: Absolute pressure fields at $k = 0.3 \times 2\pi/a$ for the interfaces. (c) Simulated absolute pressure fields at the frequency $f = 7500$ Hz (within the topological band gap) along the interfaces between two TIs (left panel, structure I) and through the bulk TI (right panel, structure II). (d) Experimentally measured transmission spectra of topological edge states and bulk states. (e) Simulated and measured pressure amplitude profile of a cutline in the middle of the crystal [red dashed line in (c)] at the frequency $f = 7500$ Hz. FWHM $= 1.2a$, where a is the lattice constant. (f) Experimentally detected frequency-dependent spatial profile of the absolute pressure fields measured in the middle of the crystal [red dashed line in (c)]. The zero of the scanning axis is set at the interface between two TIs.

constant. As shown in Fig. 2(f), we scan the pressure field along the cutline within the frequency range of the topological band gap, which indicates that the tightness of the edge states indeed is insensitive to frequency.

C. Effects of lattice-scale defects

The key manifestation of acoustic topological insulators is the reflection-free transmission of excited edge states. However, in principle, the lattice-scale defects can couple to different valleys and, thus, introduce backscattering to the counterpropagating modes in topological valley insulators. As a proof of principle, we deliberately introduce three types of lattice-scale defects (Fig. 3) and investigate their influences: (1) bends containing sharp corners, (2) strong local disorder in the lattice achieved by swapping erected and upside-down TLRs, and (3) a resonant cavity formed by removing rods. A continuous sinusoidal sound wave radiates normally into the waveguide. The degree of backscattering can be observed in the absolute pressure field maps, as shown in Figs. 3(a)–3(d). Figure 3(b) shows a negligible reflection of the topological edge states with four sharp bends. However, the strong local disorder and the cavity entail significant wave backscattering at the local defects resulting in increased sound reflections. Figure 3(e) further shows the experimental measured transmission spectra for a topological protected waveguide (TPWG). Sound propagations along the interface with bends are marginally affected only within the frequency range of 8959–9450 Hz (yellow-shadowed region), which is the spectral forbidden regime for the positive interface; see Fig. 2(b). The other defects, especially the cavity, severely inhibit the forward propagation, leading to a significantly decreased transmission or even a total reflection. The effects of the different degrees of defects are also investigated in Appendix E. To sum up, the sharp turns induce

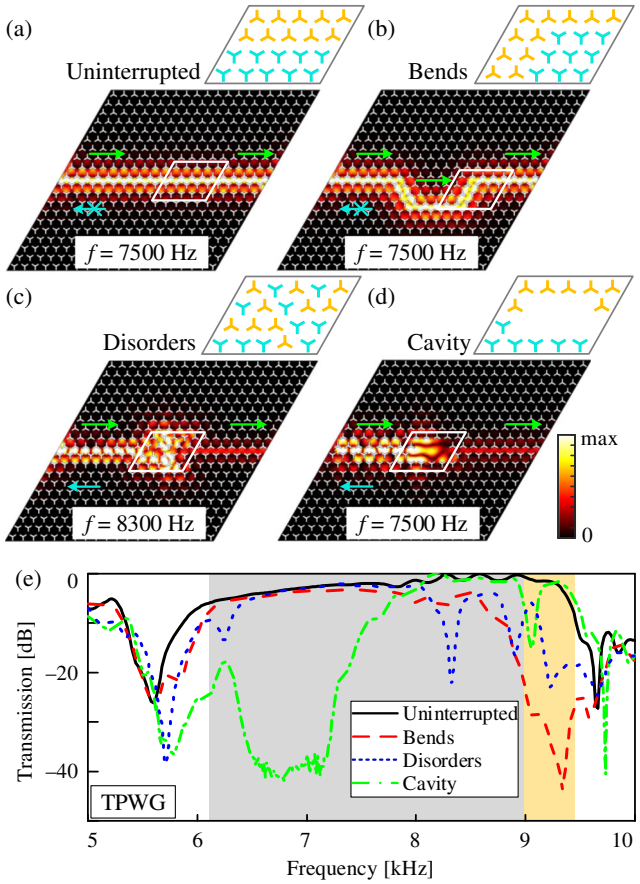

FIG. 3. Robustness of the topologically protected waveguide against different defects. Simulated absolute pressure fields in the TPWG (a) without defects (uninterrupted) and with three kinds of defects: (b) bends, (c) disorder, and (d) a cavity, respectively. Green and cyan arrows denote the directions of transmitted and reflected sound waves. Inset: Magnification of the uninterrupted interface and the interfaces with three kinds of defects. (e) Experimental transmission spectra for TPWG. The shaded regions represent the frequency region of the topological band gap. The yellow region is the forbidden band for the positive interface.

very little backscattering; however, the presence of lattice-scale defects, especially disorder and cavities, will induce intervalley scattering and decrease sound transmission. We demonstrate that although topological valley insulators are much simpler and very flexibly reconfigured as compared with the topological insulators [23–26], the robustness of the topological valley transport is weakened. A trade-off between simplicity of the implementation and robustness should be made.

D. Device implementation based on tunable topological waveguides

The reconfigurability of the structure is the cornerstone behind current acoustic functional devices and metamaterials. The tunability of the TLRs is illustrated in Fig. 1(b), in which computer-controlled motors attached to the pedestals of the TLRs can provide the desired rotation. To further corroborate this approach and to demonstrate the actual proof-of-concept based on the reconfigurable topological edge states, we engineer *topologically switchable waveguides* as shown in Fig. 4(a). Parts of the TLRs (highlighted by black color) are mounted onto computer-controlled motors. As a result, the topologically protected pathway can be easily controlled. Depending on the rotation angle selected, −30° or 30°, respectively, sound waves transmit either through port 1 or port 2 as illustrated in Fig. 4(b). We emphasize that vast possibilities of functional devices can be engineered by simply configuring the TLRs to any desired angle.

E. Time-delay lines based on topological edge states

Owing to the spectrally broad response of the TIs built using TLRs, we are able to send short pulses through PCs and engineer their dynamic behavior. The tremendous advantage of reflection-free acoustic signal transmission not yielding to sharp bends along the way enables one to design acoustic delay lines by means of topologically protected transient edge states. The robust optical delay lines have been theoretically proposed in Ref. [11]; however, the broadband and tunable delay lines based on topological acoustics have never been demonstrated before to our knowledge. As shown in Fig. 5(a), we fabricate PDDs in the form of a square-shaped detour with four sharp bends in a TPWG that generates a time delay [22]

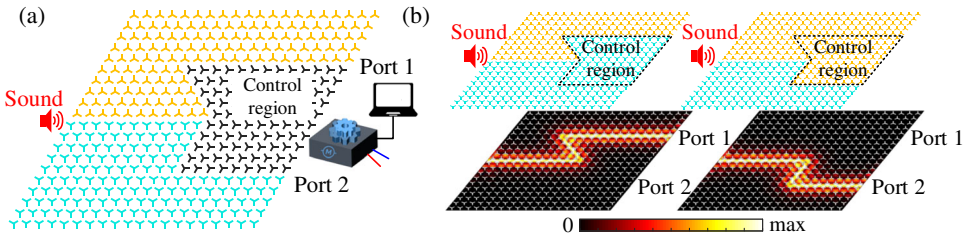

FIG. 4. Reconfigurable topological switch. (a) Setup of the reconfigurable topological switch. The pedestals of the TLRs in the black region are attached to computer-controlled motors by which the TLRs can be rotated to different angles. (b) The distributions of the pressure fields when switched between different topological states. Sound waves transmit through port 1 (port 2) at the rotation angle −30°(30°) of the reconfigurable control region [indicated by black in (a)].

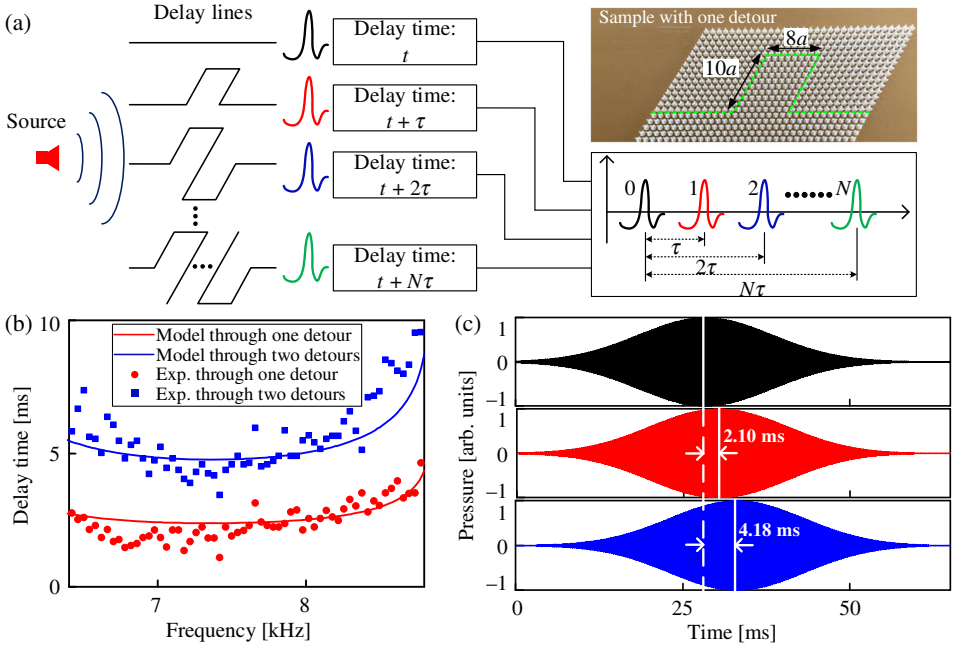

FIG. 5. Broadband delay lines based on the topological insulator. (a) The schematic of time-delay lines based on the topologically protected waveguide. The time delay of $N\tau$ can be obtained by introducing N defect detours. (b) The experimental time delays through one detour and two detours in the frequency range of 6400–8800 Hz, together with the model prediction. (c) Measured time delays through one detour and two detours with frequency $f = 7400$ Hz, in which a Gaussian-modulated sinusoidal pulse is injected. The first row shows the transmitted pressure through straight interface. The second (third) panel shows the transmitted pressure amplitude in a TI with one (two) detours.

$$\tau_i = \left(\frac{\partial\varphi_i}{\partial\omega} - \frac{\partial\varphi_0}{\partial\omega}\right) = \frac{1}{2\pi}\left(\frac{\partial\varphi_i}{\partial f} - \frac{\partial\varphi_0}{\partial f}\right), \quad i = 0, 1, 2, \ldots, N, \tag{1}$$

where $\partial\varphi_i$ is the phase of the sound wave along the interface with $i = 0, 1, 2, \ldots, N$ detours, and $\partial\varphi_0$ is the phase through the uninterrupted straight waveguides. The time delay through one detour is $\tau_1 = \tau$. One of the key characteristics of the topologically protected delay lines is their compactness, since PDDs in the form of sharp bends turn into tightly packed detours without any backscattering. The time-delay line can be increased very flexibly by stacking multiple square-shaped detours. Hence, as an example, we engineer PDDs of doubled delay time $\tau_2 = 2\tau$ by joining two such square-shaped detours. Rather than refabricating a TPWG with this desired temporal response, we simply reconfigure the lattice by rotating the respective TLRs to physically form the additional detour. According to the dispersion relations in Fig. 2(b), the sound velocity can be obtained through $c_j = 2\pi(df/dk)_j$ with $j = 1, 2$ for the negative and positive interfaces. The delay time $\tau = \sum_{j=1}^{2}(s_j/c_j)$ can be derived from Eq. (1), where s_j is the length of the transmitted line. The time delays of sound waves through a one-detour and two-detour TPWG are experimentally measured as shown in Fig. 5(b) together with the model prediction. What is worth noting is that the bandwidth of topological protection remains intact. As compared to ordinary PCs where resonances produce positive and negative delay times, in the present case [see Fig. 5(b)], for most frequencies, the time delay is spectrally flat. Figure 5(c) depicts the experimentally measured time delays through TPWGs containing PDDs of one detour and two detours. In this experiment, a Gaussian-modulated sinusoidal pulse $\cos(2\pi f_c t)\times \exp[-\sigma(t-t_0)^2]$ with $\sigma = 2.68\times10^{11}$ and $t_0 = 0.025$ s is generated. The center frequency f_c and bandwidth of the pulse are 7400 Hz and 37 Hz, respectively, which ensure that the main frequencies lie in the topological band gap. The first row shows the transmitted pressure through a straight interface. The second and third panels show the transmitted pressure through the interface with one and two detours, respectively. The delay time 4.18 ms through two detours is approximately twice 2.10 ms through one detour. These experimental results constitute the first step in building a multistage broadband topologically protected delay line capable of buffering multiple acoustic pulses.

IV. CONCLUSION

In conclusion, we experimentally realize acoustic valley pseudospin and topologically protected reconfigurable edge states in a phononic TI using three-legged epoxy resin rods, which is a common material. Such a platform provides a versatile and robust approach toward manipulating sound waves without backreflection along any desired path. In particular, the ability to independently rotate each of the rods enables flexible switching between two distinct topological configurations, which should further extend the design possibilities of future tunable acoustic topological devices. Most important, as opposed to previous findings that comprise complex and narrowband topological structures, our design based on PCs made of TLRs exhibits a particularly broad frequency response of reflectionless sound propagation ideal for ultrafast dynamics. Beyond the fundamental interests of TIs, we propose a real-world application in the context of acoustic delay lines that has the exceptional potential to be implemented for

various functions such as signal buffering and pulse processing in general.

ACKNOWLEDGMENTS

This work is supported by National Key R&D Program of China (Grant No. 2017YFA0303702), NSFC (Grants No. 11674172, No. 11574148, and No. 11474162), Jiangsu Provincial NSF (Grant No. BK20160018), the Fundamental Research Funds for the Central Universities (Grant No. 020414380001), Nanjing University Innovation and Creative Program for Ph.D. candidates (Grant No. CXCY17-11), and the Postgraduate Research & Practice Innovation Program of Jiangsu Province (Grant No. KYCX17_0020). J. C. acknowledges support from the European Research Council through the Starting Grant No. 714577 PHONOMETA and from the MINECO through a Ramón y Cajal grant (Grant No. RYC-2015-17156).

Z. Z. and Y. T. contributed equally to this work.

APPENDIX A: THREE-DIMENSIONAL DISPERSION SURFACES

Figure 6(a) shows the 3D dispersion relation through the entire first BZ of the primitive cell $\boldsymbol{C}$ of the hexagonal PC, which is composed of unperturbed cylindrical epoxy resin rods with a lattice constant $a(=2.17\ \mathrm{cm})$ and a radius r (=0.95 cm). Keeping the Γ-K mirror symmetry of the primitive cell unchanged, the unperturbed (cylindrical) epoxy resin rods are simply replaced by perturbed (three-legged) rods with the rotation angle $\varphi = 0°$, lattice constant $a = 2.17$ cm, length of the side $d = 0.85$ cm and width $h = 0.30$ cm, of which the corresponding dispersion relation is shown in Fig. 6(b). It is confirmed that in both situations, the six single Dirac cones appear at the K and K' points of the first BZ. We introduce a rotation of the perturbed (three-legged) rods from $\varphi = 0°$ to the erected configuration ($\varphi = 30°$) or upside down ($\varphi = -30°$) in order to break the mirror symmetry of the primitive cell. From the three-dimensional dispersion relation [Figs. 6(c)–6(d)], it is predicted that a controllable band gap separates different pseudospin states at the K and K' points of the first BZ.

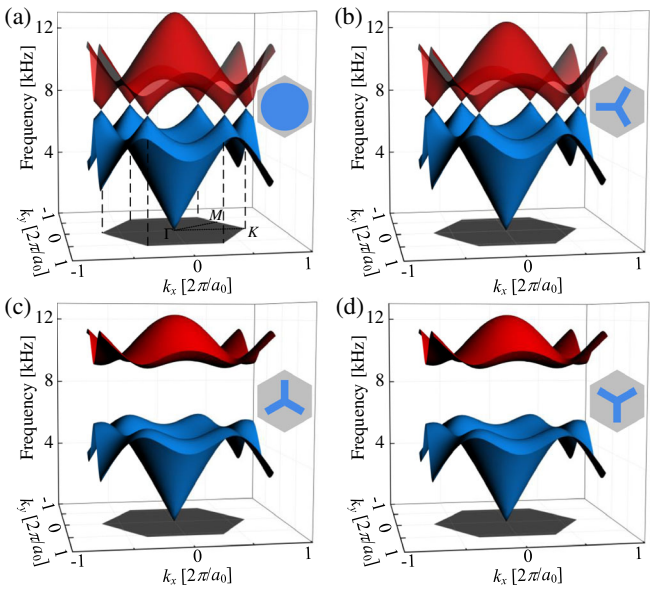

FIG. 6. 3D dispersion surfaces of hexagonal PC in the reciprocal space. Both dispersion relations for PC composed of (a) the unperturbed cylindrical and (b) the perturbed three-legged rods with a rotation angle $\varphi = 0°$ exhibit the six single Dirac cones at the K/K' points. Symmetry is broken by rotating the rod to (c) the erected configuration with $\varphi = 30°$ and (d) the upside-down one with $\varphi = -30°$.

APPENDIX B: ACHIEVING A BROADBAND TOPOLOGICAL BAND GAP

We emphasize that the ultrabroadband characteristic is specific to the proposed structure. Figure 7(a) shows the unit cell of a hexagonal PC composed of a regular triangular rod (as in Ref. [32]) with lattice constant $a = 2.17$ cm and the length of the side $d = 1.50$ cm. In this scenario, the frequency range of the band gap is $\Delta f = 2262$ Hz equal to $0.143c/a$ when normalized by $2\pi c/a$ with the sound speed in air $c = 343.20$ m/s and lattice constant a. Reducing the filling factor of the cell enlarges the band gap to $\Delta f = 2548\ \mathrm{Hz} = 0.161c/a$ [Fig. 7(b)], in which the three isosceles subtriangles are removed to obtain a Mercedes-type rod. Further, by replacing the sharp corners of the Mercedes-type rod with obtuse "legs" [Fig. 7(c)], the

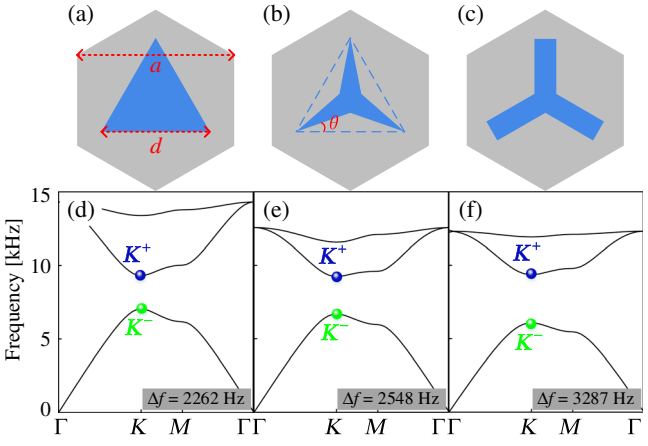

FIG. 7. Achieving a broadband topological band gap. Schematics of the unit cell of the hexagonal PC composed of (a) regular triangular rod, (b) Mercedes-type rod which is obtained by removing three isosceles subtriangles with a base angle $\theta = 23°$, and (c) three-legged rod replacing the sharp corners in (b) with obtuse legs. (d)–(f) Corresponding dispersion relations. Lower right corners: Corresponding frequency range of the band gap.

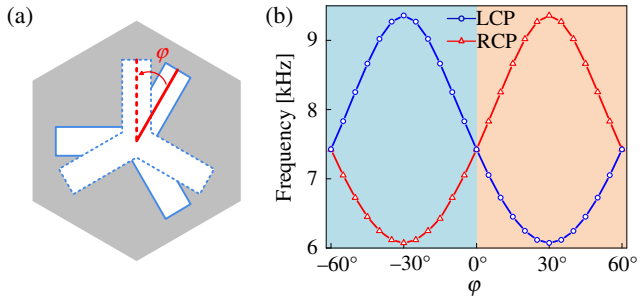

FIG. 8. Rotating the three-legged rods with band inversion. (a) Schematic of symmetry broken by rotating the rods. (b) Eigenfrequency of the two different pseudospin states dependent on the rotation angle φ at the K/K' point. The band inversion effect is clearly observed.

band gap is enlarged to $\Delta f = 3287$ Hz $= 0.208c/a$, which is almost 1.5 times larger than that of the regular triangular rod. To sum up, we demonstrate that the topological band gap can be significantly broadened by modulating the geometry of the scatterers.

APPENDIX C: BREAKING THE MIRROR SYMMETRY BY ROTATING THE THREE-LEGGED RODS

The intersection of two different pseudospin states takes place when the symmetries of the primitive cell and hexagonal lattice stay the same at which the rotating angle is $\varphi = 0^o$ as shown in Fig. 8(a). Figure 8(b) shows the topological transition in a PC with $\varphi \neq 0°$, where the eigenfrequency of pseudospin states separates the band gap at the BZ corner as a function of the rotating angle φ. The red and blue curves correspond to the RCP and LCP modes, respectively. When $\varphi < 0°$, the vortex chirality of the lower (upper) state is RCP (LCP). On the contrary, the vortex chirality of the lower (upper) state is LCP (RCP) for $\varphi > 0°$. As φ increases, the band gap closes and reopens and is accompanied by the crossing of two pseudospin states. This process is analogous to the band inversion process. Thus, as shown in Fig. 8(b), the band gap is marked with different colors to show that they have different topological characteristics.

APPENDIX D: THE EFFECTIVE HAMILTONIAN AND THE VALLEY CHERN INDICES

The effective Hamiltonian $\mathcal{H}(\boldsymbol{k}_\perp)$, which is a function of the in-plane wave number, can be expressed on the basis of the RCP or LCP states in close proximity to the K and K' points of the BZ. Because of the limited number of propagating eigenmodes being utilized, the effective Hamiltonian is an approximation, and its validity is justified only near the high-symmetry points of the BZ. Derived from the $\mathbf{k}\cdot\mathbf{p}$ theory, the unperturbed Hamiltonian $\mathcal{H}(\boldsymbol{k}_\perp) \equiv \mathcal{H}_0(\delta\boldsymbol{k})$ near the Dirac points can then be described as [3,33] $\mathcal{H}_0(\delta\boldsymbol{k}) = v_D(\delta k_x\sigma_x + \delta k_y\sigma_y)$, where v_D is the group velocity, $\delta\boldsymbol{k} = (\delta k_x, \delta k_y) \equiv \boldsymbol{k}_\perp - \boldsymbol{k}_D$ is the distance from the Dirac points with $\boldsymbol{k}_D = \pm(4\pi/3a_0)\boldsymbol{e}_x$ for the K and K' points, and $\sigma_i (i = x, y)$ are Pauli matrices of the vortex pseudospins.

Furthermore, we introduce the perturbation of the three-legged rods with two different symmetry-broken geometries (erected and upside down). The perturbation matrix is diagonalized: $\mathcal{H}_P = \omega_D\Delta_P\sigma_z$. We can obtain the band structure of the perturbed system by calculating the eigenfrequency $\Omega(\delta\boldsymbol{k}) \equiv \omega(\delta\boldsymbol{k}) - \omega_D$ of the matrix equation $\mathcal{H}(\delta\boldsymbol{k})\Psi \equiv \Omega(\delta\boldsymbol{k})\Psi$, in which $\mathcal{H} = \mathcal{H}_0 + \mathcal{H}_P$. The perturbation strength Δ_P can be determined from the first-order perturbation theory: $\Delta_P = \frac{1}{2}\int_V \Delta[1/K(\boldsymbol{r}_\perp)]\times(|p^R|^2 - |p^L|^2)dV$, where ΔV is the perturbed volume, $\Delta[1/K(\boldsymbol{r}_\perp)] = \pm[(1/K_{\text{epoxy resin}}) - (1/K_{\text{air}})]$ is the changing bulk elastic modulus after perturbation (circular to a TLR), and $p^R(p^L)$ represents the pressure of the RCP (LCP) state. The $\pm$sign of $\Delta[1/K(\boldsymbol{r}_\perp)]$ depends on whether the air region is replaced by epoxy resin or vice versa. From Fig. 1(f), we deduce the sign of the perturbation strength Δ_P depending on the orientation of the three-legged rod (the rotation angle φ). For example, the erected rod has the most negative Δ_P, whereas the upside-down rod has the largest positive Δ_P.

Although the band structures and eigenfrequencies $\Omega(\delta\boldsymbol{k})$ of the perturbed system with the opposite signs of Δ_P are identical to each other, the topological valley indices of the propagating modes in these two PC structures are not. The nontrivial topological properties of the modes can be characterized by the nonvanishing valley Chern indices [48,56,57]. By definition [48,58], $C^{(v)} = \int_{\text{BZ}(v)} d^2\delta\boldsymbol{k}[\boldsymbol{\nabla}_{\delta\boldsymbol{k}} \times \boldsymbol{A}(\delta\boldsymbol{k})]/2\pi$ with the local Berry connection [59,60] $\boldsymbol{A}(\delta\boldsymbol{k}) = -i\psi_v^\dagger(\delta\boldsymbol{k}) \cdot \boldsymbol{\nabla}_{\boldsymbol{k}}\psi_v(\delta\boldsymbol{k})$, where $v = K$, K' is the BZ corner. The integral of the Berry curvature over the full BZ is zero with the Chern number $C = 0$, which is required by time-reversal symmetry. However, for small perturbation Δ_P, the Berry curvature is strongly peaked at the gap minima near K and K'. As a result, BZ(v) is one-half of the Brillouin zone, where $k_x > 0$ for $v = K$ and $k_x < 0$ for $v = K'$ in the formula. The integral of the Berry curvature over an individual valley is accurately defined, and the nonvanishing valley Chern indices can be determined by $2C^{(K,K')} = \pm 1 \times \text{sgn}(\Delta_p)$ [48].

APPENDIX E: EFFECT OF LATTICE-SCALE DEFECTS

Short-range defects will couple to different valleys and, thus, introduce backscattering to the counterpropagating modes. This type of backscattering can, in principle, occur for any sharp feature. It has been proved that the sharp bends induce very little backscattering in Fig. 3 and Ref. [32]. However, the effects of other types of defects

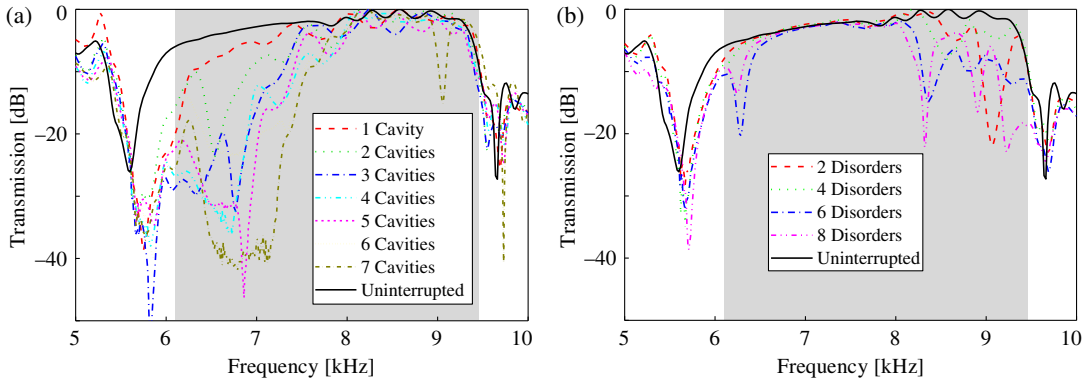

FIG. 9. Effect of topological edge states introduced by lattice-scale defects. Experimental transmission spectra for topological edge states (a) with different numbers of cavities and (b) with different numbers of disorders around the interface. The shaded regions represent the frequency region of the topological band gap.

have not been discussed. To quantify the effects of lattice-scale defects, we consider an interface between two valley Hall insulators with different numbers of cavities and disorder, which are placed near the interface. Experimental transmission spectra of helical edge states with different cavities or disorder (number of swapped erected and upside-down TLRs) are shown in Figs. 9(a) and 9(b), respectively. The decreased transmission through the interfaces with cavities or disorder demonstrates that lattice-scale defects induce backscattering and that this effect is enhanced with enlarging the area of defects. Cavities mainly have influence on the lower frequency range of the topological band gap. On the contrary, disorder mostly makes an impact on the upper frequency range.

APPENDIX F: NUMERICAL CALCULATIONS

Numerical simulations are implemented using COMSOL Multiphysics, a finite-element analysis and solver software. The simulations are performed in the pressure acoustic module including the detailed microstructures with actual geometric dimensions. The standard hard-wall boundary conditions are applied to the rods. The matrix material applied is air (25 °C) with standard parameters of a mass density $\rho_{\mathrm{air}} = 1.20\ \mathrm{kg/m^3}$ and a sound speed $c_{\mathrm{air}} = 343.20\ \mathrm{m/s}$. The largest mesh element size is lower than one-tenth of the shortest incident wavelength. Plane-wave radiation conditions are imposed on the exterior of the air domain to eliminate interference from the reflected waves. In the uniaxial structure, the acoustic eigenmodes propagate in the (x, y) plane. The representative field component can be thereby expanded with the Bloch ansatz,

$$P_z(\boldsymbol{r}_\perp, t) = \sum_{n,\boldsymbol{k}_\perp} a^n(\boldsymbol{k}_\perp) p_z^{n,\boldsymbol{k}_\perp}(\boldsymbol{r}_\perp) e^{i\boldsymbol{k}_\perp \boldsymbol{r}_\perp - i\omega_n(\boldsymbol{k}_\perp)t} + \mathrm{c.c.}, \quad \text{(F1)}$$

where the $n = 1$ (2) index refers to lower (upper) propagation band, and $p_z^{n,\boldsymbol{k}_\perp}$ is the normalized field profiles chosen to be periodic in the $\boldsymbol{r}_\perp = (x, y)$ plane. The normalized velocity field components of the modes can be obtained from Eq. (F1) as shown in the following relation:

$$v_\perp^{n,\boldsymbol{k}_\perp}(\boldsymbol{r}_\perp) = \frac{-i}{\rho(\boldsymbol{r}_\perp)\omega_n(\boldsymbol{k}_\perp)} \times [(ik_x + \partial_x) p_z^{n,\boldsymbol{k}_\perp} \hat{x} + (ik_y + \partial_y) p_z^{n,\boldsymbol{k}_\perp} \hat{y}]. \quad \text{(F2)}$$

The eigenfrequencies $\omega_n(\boldsymbol{k}_\perp)$ of the relevant modes can be calculated by using COMSOL Multiphysics, as shown in Fig. 1, where $\boldsymbol{k}_\perp = (k_x, k_y)$ belongs to the first BZ.

[1] K. Vonklitzing, G. Dorda, and M. Pepper, New Method for High-Accuracy Determination of the Fine-Structure Constant Based on Quantized Hall Resistance, Phys. Rev. Lett. **45**, 494 (1980).

[2] R. B. Laughlin, Anomalous Quantum Hall Effect: An Incompressible Quantum Fluid with Fractionally Charged Excitations, Phys. Rev. Lett. **50**, 1395 (1983).

[3] C. L. Kane and E. J. Mele, Quantum Spin Hall Effect in Graphene, Phys. Rev. Lett. **95**, 226801 (2005).

[4] B. A. Bernevig, T. L. Hughes, and S.-C. Zhang, Quantum spin Hall effect and topological phase transition in HgTe quantum wells, Science **314**, 1757 (2006).

[5] D. Hsieh, D. Qian, L. Wray, Y. Xia, Y. S. Hor, R. J. Cava, and M. Z. Hasan, A topological Dirac insulator in a quantum spin Hall phase, Nature (London) **452**, 970 (2008).

[6] M. Z. Hasan and C. L. Kane, Colloquium: Topological insulators, Rev. Mod. Phys. **82**, 3045 (2010).

[7] X.-L. Qi and S.-C. Zhang, Topological insulators and superconductors, Rev. Mod. Phys. **83**, 1057 (2011).

[8] F. D. M. Haldane and S. Raghu, Possible Realization of Directional Optical Waveguides in Photonic Crystals with Broken Time-Reversal Symmetry, Phys. Rev. Lett. **100**, 013904 (2008).

[9] Z. Wang, Y. D. Chong, J. D. Joannopoulos, and M. Soljačić, Reflection-Free One-Way Edge Modes in a Gyromagnetic Photonic Crystal, Phys. Rev. Lett. **100**, 013905 (2008).

[10] Z. Wang, Y. Chong, J. D. Joannopoulos, and M. Soljacic, Observation of unidirectional backscattering-immune topological electromagnetic states, Nature (London) **461**, 772 (2009).
[11] M. Hafezi, E. A. Demler, M. D. Lukin, and J. M. Taylor, Robust optical delay lines with topological protection, Nat. Phys. **7**, 907 (2011).
[12] K. Fang, Z. Yu, and S. Fan, Realizing effective magnetic field for photons by controlling the phase of dynamic modulation, Nat. Photonics **6**, 782 (2012).
[13] A. B. Khanikaev, S. Hossein Mousavi, W.-K. Tse, M. Kargarian, A. H. MacDonald, and G. Shvets, Photonic topological insulators, Nat. Mater. **12**, 233 (2013).
[14] G. Q. Liang and Y. D. Chong, Optical Resonator Analog of a Two-Dimensional Topological Insulator, Phys. Rev. Lett. **110**, 203904 (2013).
[15] M. Hafezi, S. Mittal, J. Fan, A. Migdall, and J. M. Taylor, Imaging topological edge states in silicon photonics, Nat. Photonics **7**, 1001 (2013).
[16] L. Lu, J. D. Joannopoulos, and M. Soljacic, Topological photonics, Nat. Photonics **8**, 821 (2014).
[17] T. Ma, A. B. Khanikaev, S. H. Mousavi, and G. Shvets, Guiding Electromagnetic Waves around Sharp Corners: Topologically Protected Photonic Transport in Metawaveguides, Phys. Rev. Lett. **114**, 127401 (2015).
[18] L.-H. Wu and X. Hu, Scheme for Achieving a Topological Photonic Crystal by Using Dielectric Material, Phys. Rev. Lett. **114**, 223901 (2015).
[19] W. Gao, M. Lawrence, B. Yang, F. Liu, F. Fang, B. Béri, J. Li, and S. Zhang, Topological Photonic Phase in Chiral Hyperbolic Metamaterials, Phys. Rev. Lett. **114**, 037402 (2015).
[20] S. Xiao, F. Zhong, H. Liu, S. Zhu, and J. Li, Flexible coherent control of plasmonic spin-Hall effect, Nat. Commun. **6**, 8360 (2015).
[21] V. Peano, C. Brendel, M. Schmidt, and F. Marquardt, Topological Phases of Sound and Light, Phys. Rev. X **5**, 031011 (2015).
[22] K. Lai, T. Ma, X. Bo, S. Anlage, and G. Shvets, Experimental realization of a reflections-free compact delay line based on a photonic topological insulator, Sci. Rep. **6**, 28453 (2016).
[23] A. B. Khanikaev, R. Fleury, S. H. Mousavi, and A. Alu, Topologically robust sound propagation in an angular-momentum-biased graphene-like resonator lattice, Nat. Commun. **6**, 8260 (2015).
[24] Z. Yang, F. Gao, X. Shi, X. Lin, Z. Gao, Y. Chong, and B. Zhang, Topological Acoustics, Phys. Rev. Lett. **114**, 114301 (2015).
[25] X. Ni, C. He, X. C. Sun, X. P. Liu, M. H. Lu, L. Feng, and Y. F. Chen, Topologically protected one-way edge mode in networks of acoustic resonators with circulating air flow, New J. Phys. **17**, 053016 (2015).
[26] Z.-G. Chen and Y. Wu, Tunable Topological Phononic Crystals, Phys. Rev. Applied **5**, 054021 (2016).
[27] C. He, Z. Li, X. Ni, X.-C. Sun, S.-Y. Yu, M.-H. Lu, X.-P. Liu, and Y.-F. Chen, Topological phononic states of underwater sound based on coupled ring resonators, Appl. Phys. Lett. **108**, 031904 (2016).
[28] Y.-G. Peng, C.-Z. Qin, D.-G. Zhao, Y.-X. Shen, X.-Y. Xu, M. Bao, H. Jia, and X.-F. Zhu, Experimental demonstration of anomalous Floquet topological insulator for sound, Nat. Commun. **7**, 13368 (2016).
[29] R. Fleury, A. B. Khanikaev, and A. Alu, Floquet topological insulators for sound, Nat. Commun. **7**, 11744 (2016).
[30] J. Mei, Z. Chen, and Y. Wu, Pseudo-time-reversal symmetry and topological edge states in two-dimensional acoustic crystals, Sci. Rep. **6**, 32752 (2016).
[31] C. He, X. Ni, H. Ge, X.-C. Sun, Y.-B. Chen, M.-H. Lu, X.-P. Liu, and Y.-F. Chen, Acoustic topological insulator and robust one-way sound transport, Nat. Phys. **12**, 1124 (2016).
[32] J. Lu, C. Qiu, L. Ye, X. Fan, M. Ke, F. Zhang, and Z. Liu, Observation of topological valley transport of sound in sonic crystals, Nat. Phys. **13**, 369 (2017).
[33] C. Brendel, V. Peano, O. J. Painter, and F. Marquardt, Pseudomagnetic fields for sound at the nanoscale, Proc. Natl. Acad. Sci. U.S.A. **114**, E3390 (2017).
[34] Z. Zhang, Q. Wei, Y. Cheng, T. Zhang, D. Wu, and X. Liu, Topological Creation of Acoustic Pseudospin Multipoles in a Flow-Free Symmetry-Broken Metamaterial Lattice, Phys. Rev. Lett. **118**, 084303 (2017).
[35] Q. Wei, Y. Tian, S. Y. Zuo, Y. Cheng, and X. J. Liu, Experimental demonstration of topologically protected efficient sound propagation in an acoustic waveguide network, Phys. Rev. B **95**, 094305 (2017).
[36] B.-Z. Xia, T.-T. Liu, G.-L. Huang, H.-Q. Dai, J.-R. Jiao, X.-G. Zang, D.-J. Yu, S.-J. Zheng, and J. Liu, Topological phononic insulator with robust pseudospin-dependent transport, Phys. Rev. B **96**, 094106 (2017).
[37] R. Suesstrunk and S. D. Huber, Observation of phononic helical edge states in a mechanical topological insulator, Science **349**, 47 (2015).
[38] S. H. Mousavi, A. B. Khanikaev, and Z. Wang, Topologically protected elastic waves in phononic metamaterials, Nat. Commun. **6**, 8682 (2015).
[39] L. M. Nash, D. Kleckner, A. Read, V. Vitelli, A. M. Turner, and W. T. M. Irvine, Topological mechanics of gyroscopic metamaterials, Proc. Natl. Acad. Sci. U.S.A. **112**, 14495 (2015).
[40] R. Fleury, D. L. Sounas, C. F. Sieck, M. R. Haberman, and A. Alù, Sound isolation and giant linear nonreciprocity in a compact acoustic circulator, Science **343**, 516 (2014).
[41] D. Xiao, W. Yao, and Q. Niu, Valley-Contrasting Physics in Graphene: Magnetic Moment and Topological Transport, Phys. Rev. Lett. **99**, 236809 (2007).
[42] A. Rycerz, J. Tworzydlo, and C. W. J. Beenakker, Valley filter and valley valve in graphene, Nat. Phys. **3**, 172 (2007).
[43] I. Martin, Y. M. Blanter, and A. F. Morpurgo, Topological Confinement in Bilayer Graphene, Phys. Rev. Lett. **100**, 036804 (2008).
[44] G. W. Semenoff, V. Semenoff, and F. Zhou, Domain Walls in Gapped Graphene, Phys. Rev. Lett. **101**, 087204 (2008).
[45] Y. Zhang, T.-T. Tang, C. Girit, Z. Hao, M. C. Martin, A. Zettl, M. F. Crommie, Y. R. Shen, and F. Wang, Direct observation of a widely tunable bandgap in bilayer graphene, Nature (London) **459**, 820 (2009).
[46] W. Yao, S. A. Yang, and Q. Niu, Edge States in Graphene: From Gapped Flat-Band to Gapless Chiral Modes, Phys. Rev. Lett. **102**, 096801 (2009).

[47] F. Zhang, J. Jung, G. A. Fiete, Q. A. Niu, and A. H. MacDonald, Spontaneous Quantum Hall States in Chirally Stacked Few-Layer Graphene Systems, Phys. Rev. Lett. **106**, 156801 (2011).

[48] F. Zhang, A. H. MacDonald, and E. J. Mele, Valley Chern numbers and boundary modes in gapped bilayer graphene, Proc. Natl. Acad. Sci. U.S.A. **110**, 10546 (2013).

[49] J. Lu, C. Qiu, M. Ke, and Z. Liu, Valley Vortex States in Sonic Crystals, Phys. Rev. Lett. **116**, 093901 (2016).

[50] R. K. Pal and M. Ruzzene, Edge waves in plates with resonators: an elastic analogue of the quantum valley Hall effect, New J. Phys. **19**, 025001 (2017).

[51] F. Guinea, M. I. Katsnelson, and A. K. Geim, Energy gaps and a zero-field quantum Hall effect in graphene by strain engineering, Nat. Phys. **6**, 30 (2010).

[52] M. C. Rechtsman, J. M. Zeuner, A. Tünnermann, S. Nolte, M. Segev, and A. Szameit, Strain-induced pseudomagnetic field and photonic Landau levels in dielectric structures, Nat. Photonics **7**, 153 (2013).

[53] P. Dziawa, B. J. Kowalski, K. Dybko, R. Buczko, A. Szczerbakow, M. Szot, E. Łusakowska, T. Balasubramanian, B. M. Wojek, M. H. Berntsen, O. Tjernberg, and T. Story, Topological crystalline insulator states in $Pb_{1-x}Sn_xSe$, Nat. Mater. **11**, 1023 (2012).

[54] M. Xiao, G. Ma, Z. Yang, P. Sheng, Z. Q. Zhang, and C. T. Chan, Geometric phase and band inversion in periodic acoustic systems, Nat. Phys. **11**, 240 (2015).

[55] Y. Yang, Z. Xu, L. Sheng, B. Wang, D. Y. Xing, and D. N. Sheng, Time-Reversal-Symmetry-Broken Quantum Spin Hall Effect, Phys. Rev. Lett. **107**, 066602 (2011).

[56] M. Ezawa, Topological Kirchhoff law and bulk-edge correspondence for valley Chern and spin-valley Chern numbers, Phys. Rev. B **88**, 161406 (2013).

[57] M. Ezawa, Symmetry protected topological charge in symmetry broken phase: Spin-Chern, spin-valley-Chern and mirror-Chern numbers, Phys. Lett. A **378**, 1180 (2014).

[58] M. Tzuhsuan and S. Gennady, All-Si valley-Hall photonic topological insulator, New J. Phys. **18**, 025012 (2016).

[59] D. J. Thouless, M. Kohmoto, M. P. Nightingale, and M. den Nijs, Quantized Hall Conductance in a Two-Dimensional Periodic Potential, Phys. Rev. Lett. **49**, 405 (1982).

[60] B. Simon, Holonomy, the Quantum Adiabatic Theorem, and Berry's Phase, Phys. Rev. Lett. **51**, 2167 (1983).